RESEARCH ARTICLE

An Improved Path-Loss Model for Reconfigurable-Intelligent-Surface-Aided Wireless Communications and Experimental Validation

JUNGI JEONG[ID], JUN HWA OH, SEUNG YOON LEE, YUNTAE PARK, AND SANG-HYUK WI
Samsung Research, Samsung Electronics Company, Seoul 06765, South Korea

Corresponding author: Sang-Hyuk Wi (sang-hyuk.wi@samsung.com)

ABSTRACT Recently, a reconfigurable intelligent surface (RIS) that provides alternative wireless propagation paths (by reflecting an electromagnetic wave from a base station in desired directions) has attracted attention as a key facilitating technology for Beyond 5G and 6G wireless communications. This paper presents an improved path-loss model suitable for RIS-aided wireless communications. Unlike previously reported RIS path-loss models, the proposed model considers more practical electromagnetic phenomena (e.g., the incident and reflected gain patterns of the RIS unit cell, the effective received power at the RIS, the reflection phase error of each unit cell, and the specular reflection loss), by applying rigorous analysis. Furthermore, the accuracy of the proposed path-loss model is validated by extensive experimental measurements using our developed RIS prototype. The prototype consists of 576 phase-reconfigurable unit cells operating at 29 GHz, each of which features two PIN diodes. Each PIN diode is independently controlled to produce the desired phase distributions on the RIS. It is shown that the calculated received power in the proposed path-loss model matches the measurement results within a 1 dB margin across various practical test environments.

INDEX TERMS Metasurface, millimeter wave, path-loss model, reconfigurable reflector, reconfigurable intelligent surface (RIS), wireless communication system.

I. INTRODUCTION

IMT-2020, also known as 5th generation (5G) wireless mobile communications, became commercially available in 2019, including operations in millimeter-wave (mmWave) frequency bands between 24.25 GHz and 52.6 GHz, referred to as Frequency Range 2 (FR2). In general, 5G FR2 has the advantage of being able to support new mobile applications that demand extremely high data rates, thanks to the wide range of channel bandwidths available (as large as several hundreds of MHz). Despite the more severe path loss in the FR2 bands (compared to the microwave frequency bands), massive multiple-input and multiple-output (MIMO) antenna systems featuring advanced beamforming technologies in 5G

The associate editor coordinating the review of this manuscript and approving it for publication was Barbara Masini[ID].

can provide an improved end-user experience with enhanced coverage and spectral efficiency. Therefore, numerous studies have been conducted on mmWave beamforming systems [1], [2], [3], [4], [5], [6], [7], [8], [9], [10], [11].

However, the coverage hole problem in a non-line-of-sight (NLOS) environment remains difficult to solve, even with the advanced beamforming technologies of 5G FR2 bands, as explained below. The coverage hole is an area in a wireless communications network where data transmission is not achievable because of arbitrary obstacles. When the high-frequency signal reaches an arbitrary object, the roughness of the object surface appears larger than that observed under the legacy microwave frequency signals. Accordingly, the wireless propagation paths permitted via reflection and diffraction from these objects are reduced. As a result, in 5G FR2, base stations must be deployed more densely than in

lower-frequency cellular networks. In addition, this coverage-hole problem is not limited to 5G New Radio FR2. A similar problem is expected to occur in subsequent 6G wireless communications, which may employ even higher frequency bands (e.g., the sub-terahertz bands) and wider bandwidths to realize emerging data-intensive applications such as immersive extended reality, high-fidelity mobile holograms, and digital replicas [12]. Many "6G White Papers" have proposed diverse technologies to solve this problem, and numerous studies have been actively undertaken [12], [13], [14], [15], [16], [17], [18], [19], [20].
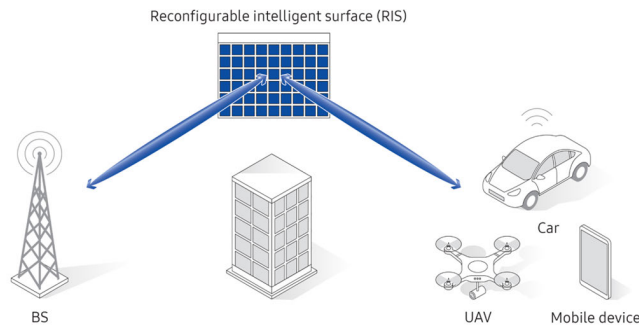

FIGURE 1. RIS-aided wireless communication [12].

One technique introduced in a white paper [12] to solve the coverage hole problem was a reconfigurable intelligent surface (RIS). A RIS, defined as an actively controlled metasurface, can provide alternative wireless propagation paths when new ones are required, as shown in Fig. 1. When obstacles block the line-of-sight paths between the base station and user equipment, alternative paths can be provided to users in the blocked area via the reflected signal at the RIS. The RIS consists of uniformly distributed reconfigurable unit cells with integrated switching devices (or components). The reflection phase of each unit cell can be intelligently changed by controlling the state of the integrated switching components (e.g., PIN diodes [21], [22], RF switches [23], [24], [25], varactor diodes [26], [27], liquid crystals [28], microelectromechanical systems [29], graphene [30], field effect transistors [31], and VO2s [32]).

The utility of RIS for solving coverage hole issues has been demonstrated via wireless-communication-based theoretical analysis [33], [34], [35], [36], [37], [38], [39]. The RIS can extend coverage not only outdoors but also indoors [40], considering various form factors pertaining to different environments and purposes. Moreover, the applications of RIS (asides from coverage extension) include interference management [22] and MIMO spatial channel enhancement [21].

In particular, to characterize the practical performance of RIS-aided communication systems, an accurate path-loss model involving RIS is essential. This is because the proper position and requisite size of the RIS can vary according to the performance predicted by the path-loss model. Many studies into RIS path-loss model (reported in [41], [42], [43],

and [44]) were based upon a simple mathematical model; hence, discrepancies may arise between the calculated and actual measurement results. In [45], the path-loss model was revised from an electromagnetic-theory based perspective. However, the unit cell gain pattern and received power of the RIS were not considered sufficient for practical applications. Additionally, this path loss model does not account for physical phenomena such as actual phase errors and specular reflection. This could result in an inaccurate path-loss model at certain distances and angles.

In this paper, an improved path-loss model is proposed considering practical electromagnetic phenomena that have not been accurately analyzed in previous papers; it can accurately predict the path-loss of RIS-aided communications systems. This can be used for accurate communication channel modeling or codebook design in the future [46], [47], [48]. Section II describes the proposed path-loss model and our contributions in detail. The unit cell gain pattern, received power at the RIS, unit cell phase errors, and specular reflection loss are discussed. In Section III, we design a 2-bit unit cell at 29 GHz, to implement the actual RIS and simulate the reflected beam performance according to the phase distribution of the RIS surface; to this end, we use the 3D electromagnetic simulation tool. To control the phase distribution of the RIS surface, it is necessary to control each unit cell and design shift registers and an Arduino microcontroller, as presented in Section IV. Finally, in Section V, the path-loss model proposed in Section II is verified by comparing it with experiment results obtained using the fabricated RIS prototype from Section IV.

II. PATH-LOSS MODELING

The concept of RIS-aided propagation paths is illustrated in Fig. 2. Theoretically, the electromagnetic field radiating from Tx is reflected by the unit cells in the RIS. Hence, the received power of Rx in the RIS-aided propagation path can be obtained from the product of two-divided paths (Tx to RIS and RIS to Rx). In addition, each path can be represented as the superposition of each independent propagation path of the unit cell, expressed as [45]

$$
P_r = P_t \sum_{n=1}^{N} \left[G_t \left(\theta'_n, \phi'_n \right) G_{unit} \left(\theta_{in}, \phi_{in} \right) \left(\frac{\lambda}{4\pi d_{tn}} \right)^2 \right]
$$
$$
\times \sum_{n=1}^{N} \left[G_r \left(\theta''_n, \phi''_n \right) G_{unit} \left(\theta_{rn}, \phi_{rn} \right) |\Gamma_n|^2 \left(\frac{\lambda}{4\pi d_{rn}} \right)^2 \right],
$$
(1)

where N is the number of unit cells on the RIS; P_r is the Rx-received power of the RIS-aided propagation path; primed and double-primed coordinates denote the radiation pattern of the Tx and Rx antennas, respectively; $G_t(\theta'_n, \phi'_n)$ and $G_r(\theta''_n, \phi''_n)$ are the Tx and Rx antenna gains, respectively, for the nth unit cell; $G_{unit}(\theta, \phi)$ is the gain of the unit cell and is reciprocal between incident and reflection; (θ_{in}, ϕ_{in}) and (θ_{rn}, ϕ_{rn}) are the incident and reflected angles, respectively,
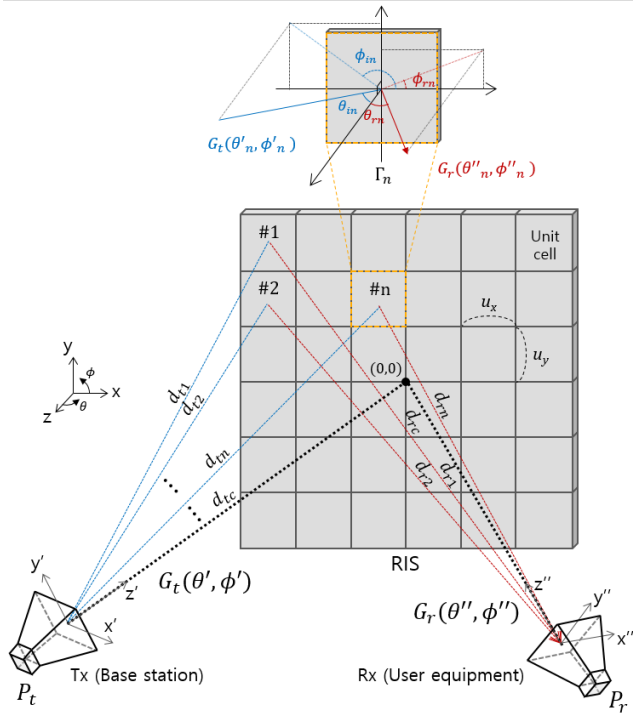
FIGURE 2. Scattering concept of RIS-aided propagation path.

of the nth unit cell; d_{tn} and d_{rn} are the distances from the nth unit cell to each Tx and Rx, respectively; and $|\Gamma_n|$ is the reflection amplitude of the nth unit cell. We assume that the polarization is always properly matched. This is a theoretical equation based upon the Friis equation; hence, it is not sufficient to accurately estimate the path loss in a RIS-aided environment. To increase the accuracy of the equation, detailed analyses of the electromagnetic phenomena are performed from various perspectives in the following subsections, and an improved path-loss model is proposed.

A. UNIT CELL GAIN PATTERN

It is convenient to calculate the gain pattern of the unit cell using the effective aperture from antenna theory, expressed as

$$G_{unit}\left(\theta_{in}, \phi_{in}\right) = \frac{4\pi}{\lambda^2} A_e\left(\theta_{in}, \phi_{in}\right) \qquad (2.1)$$

$$G_{unit}\left(\theta_{rn}, \phi_{rn}\right) = \frac{4\pi}{\lambda^2} A_e\left(\theta_{rn}, \phi_{rn}\right) \qquad (2.2)$$

where A_e denotes the effective aperture of the unit cell. The aperture efficiency is defined as the ratio between the available power at the aperture and the power flux density of a plane wave incident upon a unit cell:

$$A_e\left(\theta_{in}, \phi_{in}\right) = \frac{P_A}{S} \qquad (3)$$

Here, P_A is the available power and S is the power flux density of the incident wave.

Because the unit cell reflects most of the electromagnetic fields radiating from the Tx antenna, most of the power incident upon the unit cell surface is available. Therefore, the
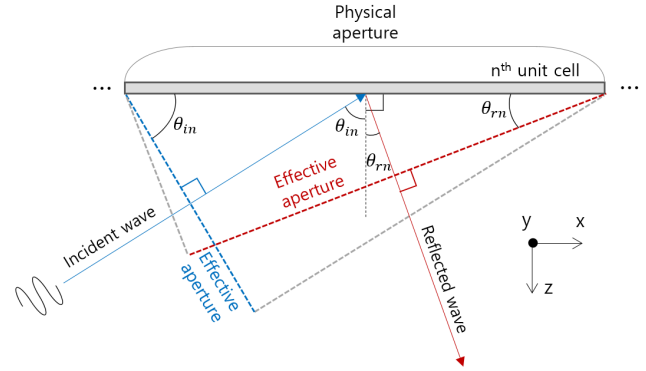

FIGURE 3. Effective aperture of the RIS unit cell with respect to the incident and reflected angles in the azimuth plane.

effective aperture of the unit cell can be determined as the projected aperture area of the unit cell from the Tx-antenna direction. In Fig. 3, the effective aperture of the unit cell is represented graphically when Tx and Rx both lie in the azimuth plane ($\phi_{in} = \phi_{rn} = 0°$). Extending this to a 3D environment, when the RIS surface is on the x-y plane, the projected aperture region of the unit cell is determined by the degree of inclination (θ_{in} or θ_{rn}) from the normal direction of the unit cell, regardless of ϕ_{in} or ϕ_{rn}. Therefore, the aperture efficiency is determined only from θ_{in} and θ_{rn}, and (2.1) and (2.2) are derived as follows:

$$\frac{4\pi}{\lambda^2} A_e\left(\theta_{in}, \phi_{in}\right) = \frac{4\pi}{\lambda^2} A_p \cos\theta_{in} \qquad (4.1)$$

$$\frac{4\pi}{\lambda^2} A_e\left(\theta_{rn}, \phi_{rn}\right) = \frac{4\pi}{\lambda^2} A_p \cos\theta_{rn} \qquad (4.2)$$

where A_P is the physical aperture area of the unit cell. In practice, each effective aperture of the unit cell is different, because θ_{in} and θ_{rn} are varied depending on the position of the cells. However, it can be assumed to be a single value base on the center point of the RIS, because the distances between the RIS and the Tx and Rx are sufficiently large in the RIS-aided environment. Consequently, the single values of the incident and reflected angles based on the RIS center (θ_{ic} and θ_{rc}) are applied to (4.1) and (4.2), and (1) can be rewritten as

$$P_r = P_t \left(\frac{A_p}{4\pi}\right)^2 \cos\theta_{ic} \cos\theta_{rc}$$
$$\times \sum_{n=1}^{N}\left[\frac{G_t\left(\theta_n', \phi_n'\right)}{d_{tn}^2}\right] \sum_{n=1}^{N}\left[\frac{G_r\left(\theta_n'', \phi_n''\right)|\Gamma_n|^2}{d_{rn}^2}\right], \qquad (5)$$

where θ_{ic} and θ_{rc} are the incident and reflected angles, respectively, based on the center of the RIS.

From (5), it can be observed that Rx receives maximum power when the reflected angle lies in the normal direction of the RIS surface at a fixed incident angle, and the received power follows the cosine of the reflected angle. Simultaneously, maximum power is received when the Tx is placed in the normal direction, and it decreases according to the cosine

of the incident angle. To summarize, Rx receives a larger power when the directions of Tx and Rx are more closely aligned to the normal direction of the RIS surface and vary according to the cosine of the incident and reflected angles.

B. EFFECTIVE RECEIVING POWER OF RIS

The RIS can be installed in various RIS-aided communication environments for different user scenarios. However, if the distance between Tx and the RIS is small or the size of the RIS is increased, the received power may differ between unit cells (as shown in Fig. 4), owing to the radiation pattern of the Tx antenna. However, the path-loss models of conventional papers assume that all unit cells on the RIS receive the same power; this is inaccurate in the above-mentioned environments and should be modified to improve accuracy across various RIS-aided environments. In this subsection, the power intensities incident upon the unit cells from the Tx antenna are accurately calculated for application to the path-loss model. These can be obtained from the radiation pattern shape of the Tx antenna and the configuration of the RIS-aided environment.
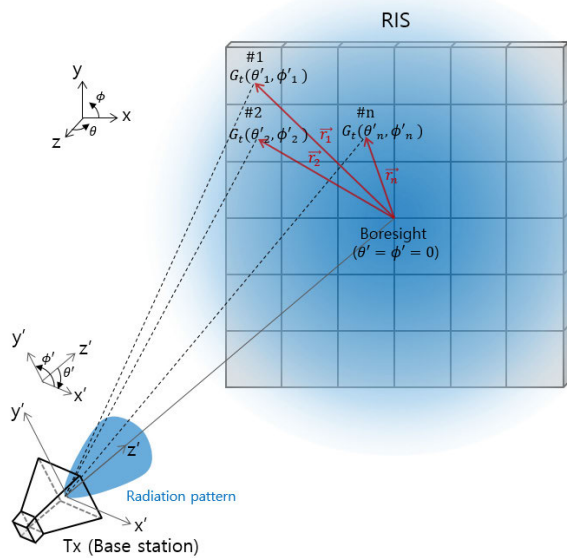

FIGURE 4. Received power intensity at the RIS surface in case of a short distance between the Tx and RIS.

First, because the antenna gain is generally given as a single value of boresight, it is necessary to compute the radiation pattern from the gain value. Theoretically, the gain pattern of the antenna can be assumed to form a rectangular radiation pattern, as shown in Fig. 5; this can be written as [49]

$$
\begin{aligned}
Gain &= \frac{Area\ of\ sphere}{Area\ of\ antenna\ pattern} \\
&= \frac{4\pi d_{BW}^2}{d_{BW}^2 \sin BW_{\theta'} \sin BW_{\phi'}} = \frac{4\pi}{\sin BW_{\theta'} \sin BW_{\phi'}},
\end{aligned}
$$

(6)

where $BW_{\theta'}$ and $BW_{\phi'}$ are the beamwidths of each axis and d_{BW} is the distance from the pattern aperture to the antenna. In general, the gain of the Tx antenna is high with a narrow beamwidth, and (6) can be rewritten as

$$
Gain = \frac{4\pi}{BW_{\theta'} BW_{\phi'}}.
$$

(7)

However, this beam pattern is impractical because it represents an ideal rectangular beam, which assumes that the antenna radiates equally in the rectangular area. In [49], the beam efficiency is applied in (7) to calculate the practical case, as

$$
\begin{aligned}
Gain &= \varepsilon_M \frac{4\pi}{BW_{\theta'} BW_{\phi'}}, \\
\varepsilon_M &= \Omega_M / \Omega_A,
\end{aligned}
$$

(8)

where ε_M is the beam efficiency, and Ω_M and Ω_A denote the beam solid angle of the main beam and overall pattern, respectively. The beam efficiency indicates the ratio between the main beam and total radiation power; it is "1" for the ideal rectangular beam pattern, as shown in Fig. 5. In other words, the beam efficiency is determined by the shape of the beam pattern and generally has a value smaller than "1". The Tx antenna is generally implemented using a planar aperture with an antenna array, and the beam efficiency can be determined as 0.6 [49]. In addition, the Tx antenna main beam pattern can be approximately defined as the cosine of θ' with a constant value for ϕ'; this is expressed as

$$
G_t(\theta', \phi') = \cos^{pt} \theta',
$$

(9)

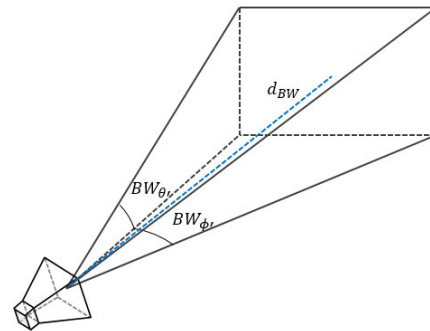where pt is determined using the beamwidth from (8).

FIGURE 5. Antenna radiation pattern approximated as rectangular.

Second, the angle of each unit cell from the Tx antenna must be calculated when applying (9). Fig. 6 shows the concept of the Tx antenna gain for the nth unit cell propagation path in the azimuth plane. When the boresight of the Tx antenna is directed towards the center of the RIS surface, the angle between the position vector of the unit cell and the Tx antenna can be written as

$$
\theta_{tn} = \cos^{-1}\left(\frac{\boldsymbol{r_n} \cdot \boldsymbol{d_{tc}}}{|\boldsymbol{r_n}||\boldsymbol{d_{tc}}|}\right),
$$

(10)

where $\boldsymbol{r_n}$ is the position vector of the nth unit cell, $\boldsymbol{d_{tc}}$ is the position vector of the Tx antenna, and θ_{tn} is the angle
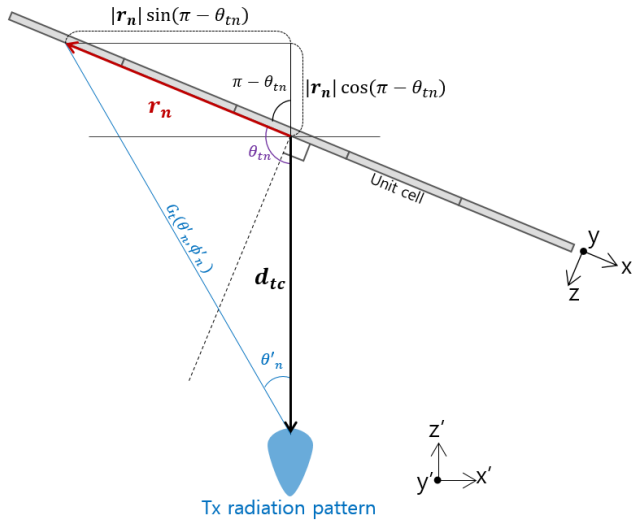
FIGURE 6. Concept of the Tx antenna gain for the n$^{\text{th}}$ unit cell propagation path in the azimuth plane.

between these two vectors. Using the calculated θ_{tn}, θ'_n can be obtained as

$$\theta'_n = \tan^{-1}\left(\frac{|\boldsymbol{r_n}|\sin(\pi - \theta_{tn})}{|\boldsymbol{d_{tc}}| + |\boldsymbol{r_n}|\cos(\pi - \theta_{tn})}\right)$$
$$= \tan^{-1}\left(\frac{|\boldsymbol{r_n}|\sin(\theta_{tn})}{|\boldsymbol{d_{tc}}| - |\boldsymbol{r_n}|\cos(\theta_{tn})}\right). \quad (11)$$

By substituting this into (9), the Tx antenna gain of the nth unit cell propagation path can be written as follows:

$$G_t\left(\theta'_n, \phi'_n\right) = \cos^{pt}\left(\tan^{-1}\left(\frac{|\boldsymbol{r_n}|\sin(\theta_{tn})}{|\boldsymbol{d_{tc}}| - |\boldsymbol{r_n}|\cos(\theta_{tn})}\right)\right) \quad (12)$$

The average of the Tx antenna gain across all propagation paths of the unit cell can be replaced with a representative value of the Tx antenna; the average is defined as

$$G_{ta} = \frac{1}{N}\sum_{n=1}^{N}\left[\cos^{pt}\left(\tan^{-1}\left(\frac{|\boldsymbol{r_n}|\sin(\theta_{tn})}{|\boldsymbol{d_{tc}}| - |\boldsymbol{r_n}|\cos(\theta_{tn})}\right)\right)\right], \quad (13)$$

where G_{ta} is the average value of the Tx antenna gain for the unit cell propagation path. In addition, the gain of the Rx antenna can also be calculated reciprocally as

$$G_{ra} = \frac{1}{N}\sum_{n=1}^{N}\left[\cos^{pt}\left(\tan^{-1}\left(\frac{|\boldsymbol{r_n}|\sin(\theta_{rn})}{|\boldsymbol{d_{rc}}| - |\boldsymbol{r_n}|\cos(\theta_{rn})}\right)\right)\right], \quad (14)$$

where G_{ra} is the average value of the Rx antenna gain for the unit cell propagation paths, θ_{rn} is the angle between the position vector of the unit cell and that of the Rx antenna, and the pattern of the Rx antenna is defined as $\cos^{pr}(\theta'')$ where pr is determined by the beamwidth. The (13) and (14) can be

applied to (5) as follows:

$$P_r = P_t\left(\frac{A_p}{4\pi}\right)^2\cos\theta_{ic}\cos\theta_{rc}G_{ta}G_{ra}\sum_{n=1}^{N}\frac{1}{d_{tn}^2}\sum_{n=1}^{N}\frac{|\Gamma_n|^2}{d_{rn}^2}. \quad (15)$$

The received power of each unit cell propagation path differs with respect to the distances from the Tx and Rx to each unit cell; however, these differences are very small. Thus, the d_{tn} and d_{rn} can be replaced by the representative single values d_{tc} and d_{rc} represented in Fig. 2, which denote the distances measured from the center of the RIS; thus, we have

$$P_r = P_t N\left(\frac{A_p}{4\pi}\right)^2\frac{\cos\theta_{ic}\cos\theta_{rc}G_{ta}G_{ra}}{d_{tc}^2 d_{rc}^2}\sum_{n=1}^{N}|\Gamma_n|^2. \quad (16)$$
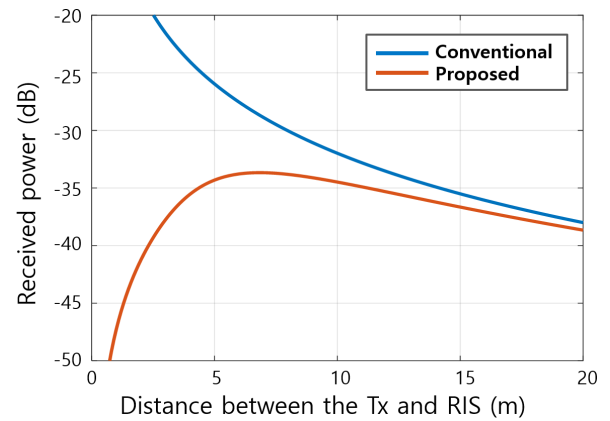

FIGURE 7. Calculated received power with respect to distance between the Tx and RIS.

To identify the difference between the proposed and conventional calculations, an example of the received power with respect to the distance between the Tx antenna and RIS is shown in Fig. 7. The calculation was performed when the Tx gain was 30 dBi, the Rx gain was 0 dBi, the RIS size was 1 m × 1 m, and the distance between the Rx and RIS was 10 m without scanning at 29 GHz.

Because the conventional path-loss model assumes that the Tx antenna gains of all unit cells are equal to the boresight gain, the received power exponentially increases when the distance between the Tx and RIS (d_{tc}) decreases, as shown in Fig. 7. However, in the proposed calculation, the received power did not increase exponentially when the distance decreased. The received power was highest at a particular distance and decreased when the distance (d_{tc}) decreased. This shows that if the distance between the RIS and Tx antenna is too small, the received power distribution on the RIS surface becomes tapered; thus, the overall received power is reduced. This result was validated by comparing measurements in last section.

C. PHASE ERROR OF UNIT CELL
Each unit cell of the RIS changes the reflection phase, and each unit cell is controlled depending on the required RIS

phase distribution, to reflect the desired beam. If the desired beam direction and location of the Tx antenna are defined, the reflection phase that compensates for the delay difference in the propagation path of each unit cell can be calculated. The distance from the phase center of the Tx antenna to each unit cell can be obtained as

$$R_n = \sqrt{|\boldsymbol{d_{tc}}|^2 + |\boldsymbol{r_n}|^2 - 2|\boldsymbol{d_{tc}}||\boldsymbol{r_n}|\cos\theta_n}, \quad (17)$$

where R_n is the distance between the nth unit cell and Tx. Subsequently, the required reflection phase of the unit cell for the plane wave in the desired direction is derived as

$$\varphi_{rn} = kR_n - k\sin\theta_r \left(r_{nx}\cos\phi_r + r_{ny}\sin\phi_r \right), \quad (18)$$

where φ_{rn} is the required reflection phase of the nth unit cell, r_{nx} is the x-axis component of r_n, r_{ny} is the y-axis component of r_n, and k is the wavenumber. However, it is difficult to ensure that the unit cell reflects tunable continuous reflection phases, because they are usually designed to have discrete values (e.g., 1-bit or 2-bit). Thus, the quantization produces a phase error depending on the number of bits (number of states) of the unit cell, and the phase error of each element can be represented as

$$\varphi_{en} = \varphi_{rn} - \varphi_q, \quad (19)$$

where φ_{en} is the phase error of the nth unit cell and φq is the closest value to φ_{rn} amongst the quantized reflection phases. This quantization error produces a gain degradation of 2–3 dB for the 1-bit case and less than 1 dB for the 2-bit one [50].
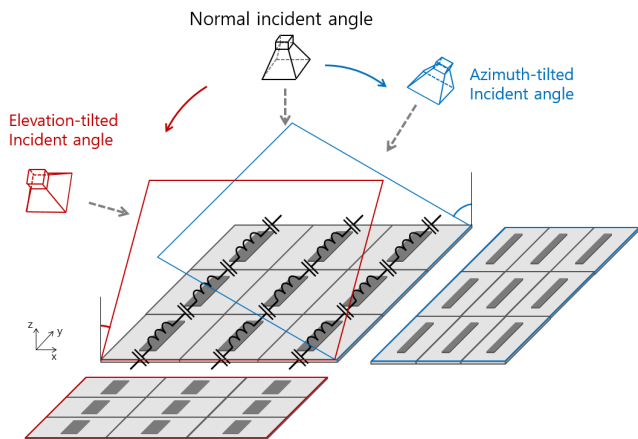

FIGURE 8. Example surface composed of periodically arranged poles and projected structure with respect to incident angle.

In addition, the phase error of the unit cell is changed according to the incident angle. In Fig. 8, an example surface composed of a periodically arranged pole is depicted to explain the reflection phase change with respect to the incident angle. The reflection phase of the unit cell is determined from the equivalent circuit characteristics of inductance and capacitance generated by the structural characteristics. However, if the incident angle is changed, the inductance and capacitance of the equivalent circuit vary because of the

difference in the projected structure generated by the incident angle. Similarly, the quantized reflection phases of the unit cell vary according to the incident angle, and the phase error is simultaneously altered. By applying this phenomenon, the phase error can be rewritten as

$$\varphi_{en}(\theta_i, \phi_i) = \varphi_{rn} - \varphi_q(\theta_i, \phi_i). \quad (20)$$

Consequently, the phase error loss is obtained from the difference in the array factor directivity of unit cells between the ideal and quantized reflection phase of the unit cells, as

$$L_{PE}(\theta_i, \phi_i, \theta_r, \phi_r) = \frac{\left| \sum_{n=1}^{N} e^{j[\varphi_{rn} + \varphi_{en}(\theta_i, \phi_i)]} \right|^2}{\left| \sum_{n=1}^{N} e^{j[\varphi_{rn}]} \right|^2}, \quad (21)$$

where $L_{PE}(\theta_i, \phi_i, \theta_r, \phi_r)$ denotes the phase-error losses with respect to the incident and reflected angles. By adding this to (16), the received power can be derived as

$$P_r = P_t N L_{PE} \left(\frac{A_p}{4\pi} \right)^2 \frac{\cos\theta_{ic} \cos\theta_{rc} G_{ta} G_{ra}}{d_{tc}^2 d_{rc}^2} \sum_{n=1}^{N} |\Gamma_n|^2. \quad (22)$$

In addition, the reflection amplitude of the unit cell can be approximated as the average value over all states, as follows:

$$P_r = P_t N^2 L_{PE} \left(\frac{A_p}{4\pi} \right)^2 \frac{\cos\theta_{ic} \cos\theta_{rc} G_{ta} G_{ra}}{d_{tc}^2 d_{rc}^2} |\Gamma_{av}|^2. \quad (23)$$
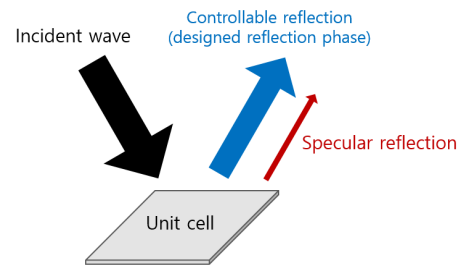

FIGURE 9. Specular reflection on the unit cell.

D. SPECULAR REFLECTION LOSS

Specular reflection is a physical phenomenon in which an electromagnetic wave is reflected (via geometric optics) back in the opposite direction when it impinges upon the reflecting material. In the RIS-aided environment, the same phenomenon occurs when the electric field is reflected by the unit cell surface, as shown in Fig. 9. Thus, the RIS surface is designed to generate the desired reflection phase via the unit cell; however, a relatively small portion of the field that cannot be controlled is also reflected. This means that although the phase distribution at the RIS is controlled for the beam scanning, the specular reflection power always remains at the specular angle. This produces a power loss when the scan angle of the RIS is not a specular reflected angle. However, when the scan angle matches the specular angle,

controllable and specular reflection can be combined. This can be added to (23) as a power-loss parameter at the reflected angle (excluding the specular reflected angle), expressed as

$$Specular\ Reflection\ Loss = L_{SR}\ (\theta_i \neq \theta_r, \phi_i \neq \phi_r), \tag{24}$$

where L_{SR} is the specular reflection loss. This loss is approximately -1 dB to -2 dB in most cases and is determined by the unit cell structure; furthermore, the value can be inferred by comparing the magnitude of the main lobe in the RIS-reflected angle with the magnitude of the specular reflection [51]. Finally, by adding (24) to (23), the received power can be derived as

$$P_r = P_t N^2 L_{PE} L_{SR} \left(\frac{A_p}{4\pi} \right)^2 \frac{\cos\theta_{ic}\cos\theta_{rc}G_{ta}G_{ra}}{d_{tc}^2 d_{rc}^2} |\Gamma_{av}|^2 . \tag{25}$$

E. PROPOSED PATH-LOSS MODEL

The received power obtained from analyses of the practical RIS-aided environment was derived in terms of the electromagnetic mechanisms in (25). This can be rewritten in the form of path loss as

$$Path\ Loss = P_t/P_r$$
$$= \frac{d_{tc}^2 d_{rc}^2 16\pi^2}{N^2 L_{PE} L_{SR} \cos\theta_{ic} \cos\theta_{rc} G_{ta} G_{ra} |\Gamma_{av}|^2 A_p^2}, \tag{26}$$

which contains most of the practical physical phenomena related to the RIS. Hence, a more accurate path loss can be obtained for various RIS-aided wireless communication scenarios. Hardware characteristics (e.g., the phase error of the unit cell and specular reflection) can be applied to produce a more practical estimate.

III. RIS PROTOTYPE DESIGN AND FABRICATION

To validate the accuracy of the proposed path-loss model, the RIS comprising 24 × 24 cross-dipole-shaped unit cells was designed to operate at 29 GHz. In previous studies [44], [45], the validity of the models was verified through experiments; however, no detailed explanation of the unit cell design was given even though the practical electromagnetic phenomena (e.g., the reflection phases of the incident and reflected angles, the phase error, and the reflection loss) should be considered. In another paper [26], a new unit cell structure was proposed as an influencing factor in RIS performance; however, the relationship between the designed RIS and path-loss model was not discussed.

This section describes the RIS unit cell design method and simulation results (e.g., the s-parameters, reflection phase variation, and RIS-reflected radiation patterns). It also includes the configuration of the RIS control board used to individually control unit cells. Finally, the RIS prototype was manufactured by integrating the designed unit cells and control circuit into one printed circuit board, and it was

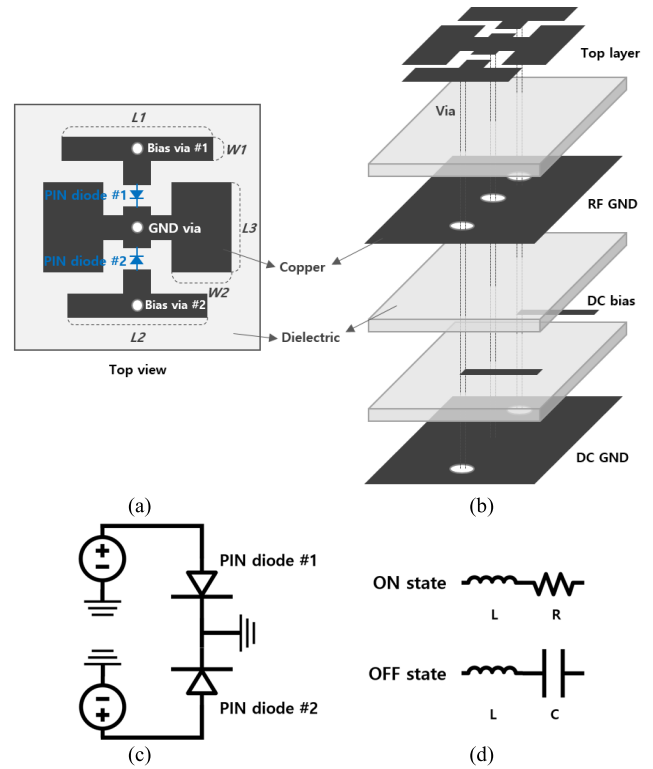confirmed that the desired phase distribution on the RIS was appropriately switched at high speeds.

FIGURE 10. Structure of the proposed 2-bit unit cell: (a) Top view, (b) exploded view, (c) DC circuit configuration of unit cell with PIN diodes, and (d) equivalent RLC model of PIN diode with respect to states.

A. UNIT CELL DESIGN

In Fig. 10(a), the black-colored structures indicate copper and the PIN diodes are denoted by blue symbols. The top-layer copper pattern of the RIS unit cell was divided into three parts, which were connected by two PIN diodes. These PIN diodes were individually controlled using the voltage control signal received from the Bias via holes #1 and #2. Both were connected to the DC GND through a center via hole. The size of the unit cell was set at 5 mm × 5 mm (less than the half-wavelength at 29 GHz) to avoid grating lobe generation. Furthermore, Fig. 10(b) shows that the proposed 2-bit unit cell was designed as a four-layer structure using the dielectric substrate Isola I-Tera MT, which has a relative permittivity of 3.45, a loss tangent of 0.0031, and a thickness of 0.78 mm.

The four quantized reflection phase states (with a 90° phase difference) can be generated by tuning the dimensions of each separated part and switching the state (ON or OFF) of PIN Diodes #1 and #2. In particular, the length difference between the two sides (*L1, L2*) is the dominant parameter for tuning the reflection phase difference of each state [52], [53].

Fig. 10(c) and (d) show the DC circuit configuration of the unit cell (with PIN diodes) and the equivalent circuit model of a diode, respectively. A MADP-000907-14020P PIN diode was used; this can be modeled as a series of lumped

resistor–inductor–capacitor (RLC) elements. When the PIN diode is in the ON state, it can be treated as a series circuit of parasitic inductances and resistances; when in the OFF state, a series circuit of parasitic inductance and capacitance is used to describe it. The geometric parameters of the unit cell are $L1 = 3.15$ mm, $L2 = 2.6$ mm, $L3 = 1.7$ mm, $W1 = 0.6$ mm, and $W2 = 1.2$ mm.

The characteristics of the proposed 2-bit reconfigurable unit cell were simulated using an ANSYS high-frequency structure simulator (HFSS). As mentioned in the previous section, the reflection phase of the unit cell is changed according to the incident angle; hence, it is necessary to determine which incident angle condition is to have a reflection difference of 90°. In our design, the target incident angle was set to $\theta_i = -45°$ and $\phi_i = 0°$, in consideration of coverage improvement for various RIS-aided wireless communications.
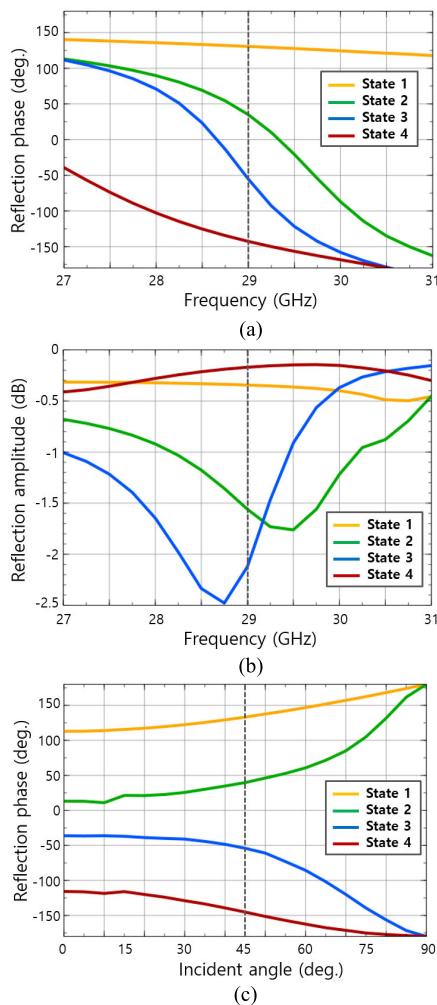
FIGURE 11. Simulated reflection coefficients of the 2-bit unit cell: (a) reflection phase, (b) reflection amplitude, and (c) reflection phase with respect to incident angle.

The simulated results of the reflection phase and the amplitude of the unit cell are presented in Fig. 11(a) and (b), respectively. The phase differences between the four states

TABLE 1. States of the unit cell.

State	State 1	State 2	State 3	State 4
Diode #1/2	ON/ON	ON/OFF	OFF/ON	OFF/OFF
Reflection phase	130.6°	34.9°	−55.3°	−142.7°

were ~90° at 29 GHz, as summarized in TABLE 1. The reflection amplitudes of the four states were −0.34 dB, −1.56 dB, −2.12 dB, and −0.17 dB at 29 GHz, respectively. The reflection amplitude of each state differed because the shape of the electromagnetic field in the unit cell varied according to the PIN diode state. The average value of these simulated reflection amplitudes was used as the magnitude of the reflection coefficient $|\Gamma_{av}|$ in (26).

The simulated reflection phases of the unit cell for incident angles of 0–90° at a frequency of 29 GHz are shown in Fig. 11(c). As predicted from the previous section, the designed phase difference changed with respect to the incident angle. This variation in the reflection phase produced a difference in the phase error loss, depending on the incident angle.
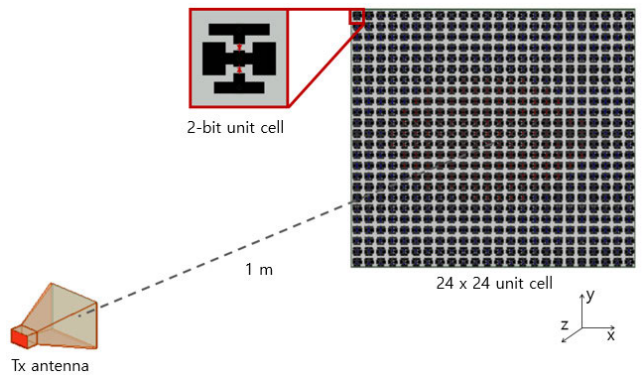
FIGURE 12. Simulation setup for verifying the RIS characteristics.

B. RIS DESIGN

To verify that the designed unit cell is suitable for RIS-aided communications, the RIS was designed as an arrangement of 24 × 24 unit cells (120 mm × 120 mm), as shown in Fig. 12. The standard horn antenna employed as the Tx antenna was placed at an angle of $\theta_i = -45°$, $\phi_i = 0°$ and a distance of 1 m from the RIS surface. The scanning capability was verified via simulation under the azimuth plane ($\phi_i = 0°$) condition, and the simulations were performed for the various reflected angles of $\theta_r = 25 - 65°$ (in intervals of 10°). The two PIN diode states of each unit cell were determined by calculating the required phase compensation value according to the steering angle and direction of the Tx antenna, as shown in (17).

The reflected gain patterns are shown in Fig. 13. The reflected peak gains are 14.82 dB, 14.77 dB, 15.46 dB,
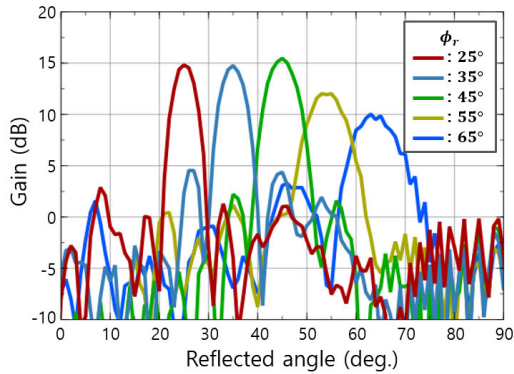
FIGURE 13. Reflected gain pattern of the RIS across various reflected angles.

FIGURE 14. Schematic of the RIS control board.

12.01 dB, and 10 dB for 25°, 35°, 45°, 55°, and 65° reflection angles, respectively. These results show that the reflected gain was highest at the specular reflected angle ($\theta_r = 45°$) compared to other angles which included the specular reflection loss. Moreover, it was observed that the reflection gain was markedly reduced when the reflected angle was varied at angles far from the normal direction ($\theta_r = 0°$) of the RIS, owing to the unit cell gain pattern.

C. RIS CONTROL BOARD DESIGN

The designed RIS is composed of 576 unit cells each equipped with two PIN diodes; in other words, it contains 1152 PIN diodes that must be controlled individually. Therefore, a control board must be designed to apply the required DC bias to the PIN diodes in the unit cells. In contrast to varactors [54], and liquid crystals [55], [56], which require multi-stage voltage control, the PIN diode has only two states (turn-on and -off voltage conditions). Hence, the control circuit can be designed simply using a commercial microcontroller instead of a complicated control circuit based upon a field-programmable gate array [57].

One of the most challenging issues when using commercial microcontrollers to operate RIS unit cells is that the number of ports on commercial microcontrollers is insufficient to control numerous PIN diodes [58]. In addition, simply using many microcontrollers causes another problem: it increases design complexity and requires a relatively large amount of space to mount. Therefore, in our design, a shift register was used to ensure an efficient control circuit configuration. The shift register is a series-input-parallel-output (SIPO) component with one data input port, eight data output ports, and two control signal ports (clock and latch). When the clock signal is high, a 1-bit value is entered through the data input and change the first output pin (Q0) to one. As the process is repeated, the values of the input port change the data output port from Q0 to Q7. The latch pin should be maintained in the low state whilst the output pins are changed according to the data input pin, and it should switch to a high state when all data transmissions are complete.
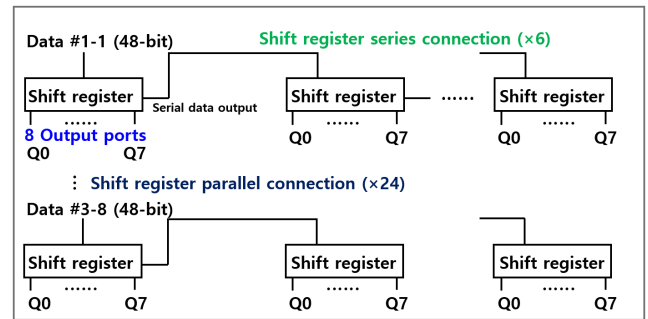
Fig. 14 shows a block diagram of the designed RIS control board. A single shift register controls the states of four 2-bit unit cells (eight PIN diodes) using an 8-bit binary data value. To implement the RIS control board more compactly, a combination of series and parallel connections in the shift registers was used.

In the case of the series connection, the serial data output port was connected to the serial data input of another shift register. These two serie's connections facilitate the transmission of 16-bit binary data and make it possible to transmit input data from a single port to eight output ports. If six shift registers are sequentially connected, the 48 PIN diodes can be controlled. This series connection can increase the number of data bits transmitted by a single data port.

Parallel connections are used to simultaneously control shift registers connected to different data ports in a microcontroller. If the microcontroller port is accessed directly, 8 or 16 ports can be manipulated simultaneously, depending on the bit number of the microcontroller used. Therefore, when using an 8-bit microcontroller (even with 24 parallel connections), the data transmission time is increased by a factor of three only, rather than 24. Consequently, the connections of the 6-series and 24-parallel shift registers are used to efficiently control a total of 1152 PIN diodes. The operating conditions of the PIN diodes and LEDs can be regulated using proper resistors by considering the current–voltage characteristics. When the RIS unit cells are turned on, each resistance (R_{PIN}, R_{G-LED}, R_{R-LED}) adjusts the current flowing through the PIN diode and LED, respectively, as shown in Fig. 15.

D. FABRICATION AND TESTING

The RIS control system was integrated with unit cells on a single board. Fig. 16(a) shows the top and bottom layers of the fabricated RIS. From the top view, we can see two PIN diodes per unit cell. At the bottom of the RIS, one shift register was implemented per four unit cells, to control eight PIN diodes. In addition, the LEDs were mounted on the bottom side of the RIS, to indicate the state of the unit cells; the 2-bit unit cell status can be confirmed from the color of the LEDs.

Fig. 16(b) shows the bottom view of the overall RIS prototype. The total PCB size was 12 cm × 18 cm, the unit cells were arranged in a 12 cm × 12 cm block, and the control circuit component for beam control was implemented
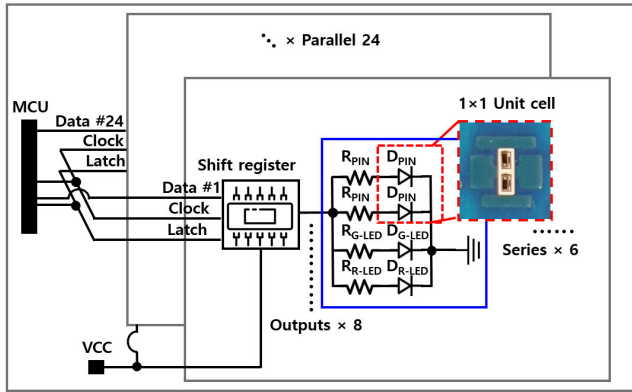
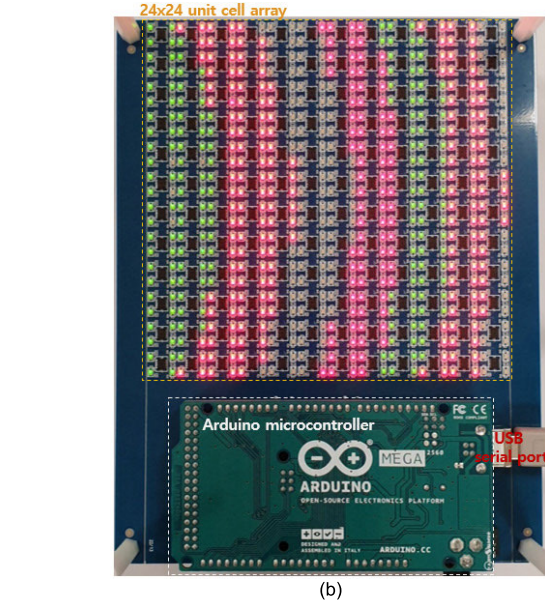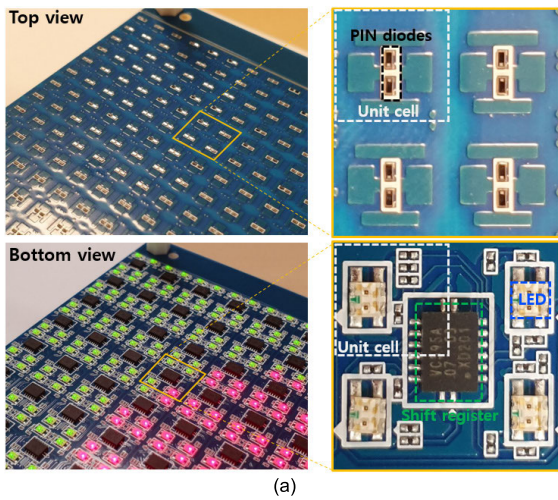**FIGURE 15.** Overall configuration of the RIS control board.

FIGURE 16. Fabricated RIS prototype: (a) configuration of the unit cells viewed at the top and bottom and (b) bottom view of the RIS (including the Arduino microcontroller board).

in the remaining 12 cm × 6 cm space. The control and DC lines were internally printed on the inner layer of the

multilayer PCB. An Atmel AVR (8-bit) CPU-based Arduino Mega 2560 was used to control the phase distribution of the RIS, and 144 shift registers consisting of 6-series and 24-parallel connections were used. As shown in Fig. 16(b), the desired phase distribution for the reflected beam was confirmed from the distribution of LED colors.

Furthermore, the data-transmission period from the Arduino to the shift register was ~0.25 μs (3.84 MHz). It took ~2 μs to convert the 8-bit data series input to the parallel output via the shift register, and a total of six series connections took 12 μs. If the coding scheme directly manipulates the ports of an 8-bit AVR, eight shift registers can be controlled simultaneously. Consequently, even though 24-parallel connections were involved, the total time required for beam switching was 36 μs.

IV. VERIFICATION OF PATH-LOSS MODEL WITH MEASURED RESULTS

Using the fabricated RIS, the proposed path-loss model was verified under various RIS-aided communication conditions (e.g., varying incident angles, reflected angles, and distances between the RIS and Tx/Rx antennas). The Tx and Rx antennas were connected to each port of the network analyzer (Keysight, N5247B), and S_{21} was measured to obtain the power decrement in the RIS-aided propagation path, as shown in Fig. 17. The connected PC controlled the states of the unit cells for the desired phase distribution. In addition, absorbers were positioned beside the Tx and Rx antennas, to eliminate the influence of direct paths therebetween.
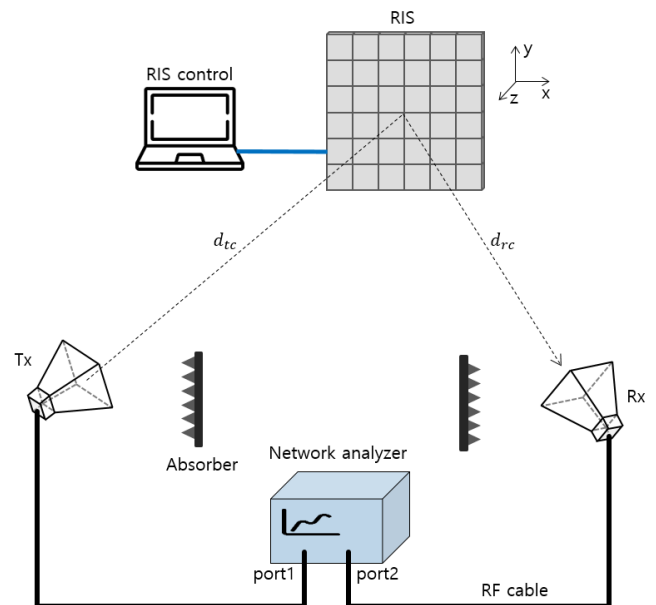

FIGURE 17. RIS measurement setup.

All experiments were conducted in an anechoic chamber to prevent unwanted interference, as shown in Fig. 18. Standard horn antennas (Eravant, SAR-1725-28KF-E2) with a 17 dBi antenna gain were used as the Tx and Rx antennas, respectively. The boresight of each horn antenna was directed at the
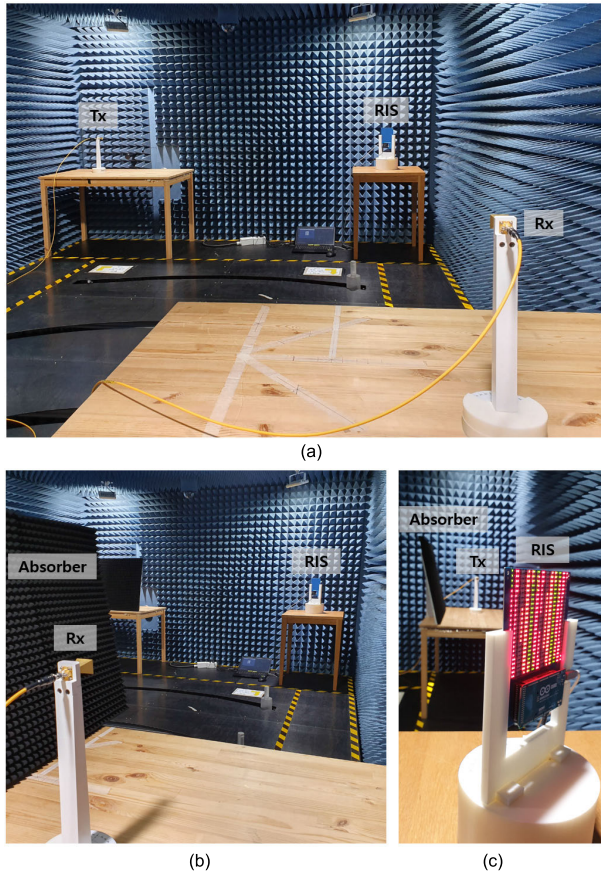
FIGURE 18. RIS measurement setup in anechoic chamber: (a) placement of Tx, Rx, and RIS in chamber; (b) Rx and RIS with the absorber; and (c) Tx and RIS with the absorber.

center of the RIS. The antennas and RIS were placed at the same height, to measure various test conditions in the azimuth plane.

Measurements were performed across three test scenarios, to prove the accuracy of the proposed path loss model. First, the received power was measured by changing the reflected angle at several fixed incident angles, to validate the accuracy of the proposed method regarding unit cell pattern, phase error loss, and specular loss. The incident angle and reflected angles were changed in the azimuth plane ($\phi_i = \phi_r = 0°$). The incident angle (θ_i) was varied from $0°$ to $45°$ with a $15°$ interval, and the reflected angle (θ_r) was varied in the range of $0°$ to $65°$ with a $5°$ interval. The Tx and Rx antennas were located 1 m from the RIS ($d_{tc} = d_{rc} = 1$m). As discussed in Section II, it was confirmed that the path losses follow the cosine of the reflected angle at all incident angles, as shown in Fig. 19(a). In addition, it can be observed that the specular loss occurred at an angle other than that of the specular direction. In addition, the received power varied as the incident angle was changed, increasing when the incident angle was closer to the normal direction of the RIS, as previously discussed. Although the measurement values were slightly lower than the calculations from the proposed path-loss model, these are strongly matched in the various incident and reflected angles.
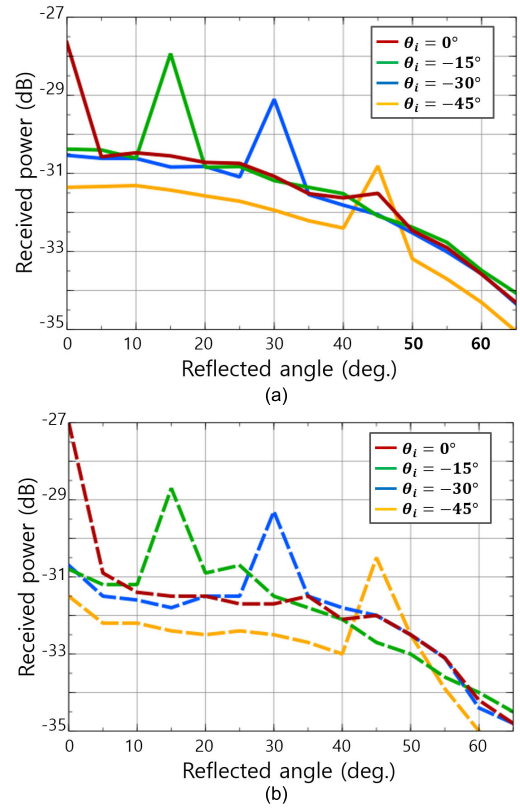

FIGURE 19. Received power at various incident and reflected angles ($\phi_i = \phi_r = 0°$): (a) proposed model calculation and (b) measurement result.
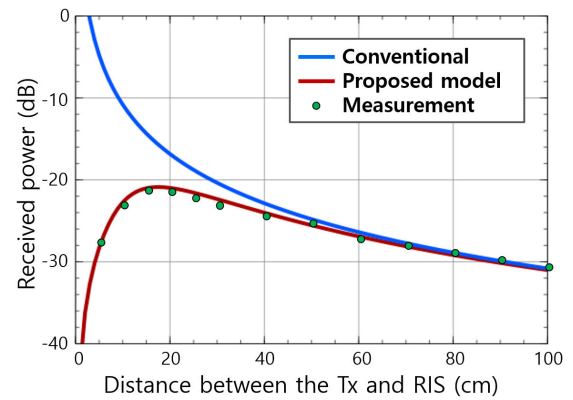

FIGURE 20. Received power with respect to distance between the Tx and RIS ($\phi_i = \phi_r = 0°, \theta_i = -45°, \theta_r = 45°$).

Second, experiments were conducted to verify the effective received power of the RIS with respect to the distance between the Tx and RIS. The received power of the Rx was measured when the distance between the Tx and RIS was reduced from 1 m. The incident and reflected angles were set as $-45°$ and $45°$ ($\theta_i = -45°, \theta_r = 45°$), respectively. The measurement results in Fig. 20 show that the received power decreased after a specific distance, as seen in the proposed model. Therefore, it is confirmed that the path loss can be predicted more accurately using the proposed path-loss

model when the RIS is deployed in an environment in which the power received on the RIS is tapered.
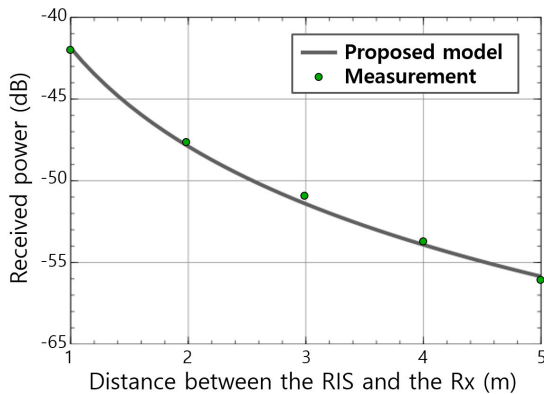

FIGURE 21. Received power with respect to distance between the RIS and Rx ($d_b = 3$ m, $\phi_i = \phi_r = 0°$, $\theta_i = -45°$, $\theta_r = 25°$).

Third, the path loss was measured at various distances between the RIS and Rx (with a 1 m interval), as shown in Fig. 21. The incident and reflected angles were fixed at $\theta_i = -45°$ and $\theta_r = 25°$, respectively. The distance between the Tx and RIS was 3 m. As the distance between the RIS and Rx increased, the received power decreased as the square of the distance, and the values corresponded with those of the path-loss model.

By comparing the measurement values and proposed model predictions, it is shown that the measured values for various RIS-aided wireless communication scenarios accurately match the proposed model calculations. The error between the proposed model and measurement was within 1 dB.

V. CONCLUSION

This study primarily sought to derive an improved path-loss model for RIS-aided wireless communications, and to conduct experimental validation. The proposed model contained four critical parameters that have not been precisely considered in previous path-loss models: 1) the incident and reflected gain patterns of the RIS unit cells, 2) the effective received powers, 3) the phase error of each unit cell, and 4) the specular reflection loss. These parameters cannot be neglected in path-loss-based performance evaluations for the realization, deployment, and operation of the RIS. The effects of all parameters were thoroughly analyzed in terms of electromagnetic phenomena before application.

Moreover, the RIS consisting of 24 × 24 cross-dipole-shaped unit cells was designed and simulated, considering actual operation and measurement conditions. The four states (with a 90° phase difference in the unit cell) and the reflection gain of the RIS were confirmed via 3D EM simulations. In addition, the RIS phase control system composed of a microcontroller and 144 shift registers with 6-series and 24-parallel connections was developed to efficiently control the 1152 PIN diodes. Subsequently, the RIS prototype was fabricated for validation. The measurement results obtained

in an anechoic chamber showed excellent agreement with the results calculated using the proposed path-loss model. Consequently, we confirmed that the proposed path-loss model can provide an accurate performance estimation for RIS-aided communications in various indoor and outdoor deployment scenarios in which direct communication paths between the transmitter and receiver systems are unavailable.

REFERENCES

[1] O. Jo, J.-J. Kim, J. Yoon, D. Choi, and W. Hong, "Exploitation of dual-polarization diversity for 5G millimeter-wave MIMO beamforming systems," *IEEE Trans. Antennas Propag.*, vol. 65, no. 12, pp. 6646–6655, Dec. 2017.

[2] D. Jung, C. Park, J. Seo, T. Kwon, J. Jeong, S. Wi, I. Na, and S. Choi, "Stub-loaded sub-terahertz wideband antenna design and measurement," in *Proc. 16th Eur. Conf. Antennas Propag. (EuCAP)*, Madrid, Spain, Mar. 2022, pp. 1–4.

[3] X. Gu, D. Liu, Y. Hasegawa, K. Masuko, C. Baks, Y. Suto, Y. Fujisaku, B. Sadhu, A. Paidimarri, N. Guan, and A. Valdes-Garcia, "Antenna-in-package integration for a wideband scalable 5G millimeter-wave phased-array module," *IEEE Microw. Wireless Compon. Lett.*, vol. 31, no. 6, pp. 682–684, Jun. 2021.

[4] B. Yu, Z. Qian, C. Lin, J. Lin, Y. Zhang, G. Yang, and Y. Luo, "A wideband mmWave antenna in fan-out wafer level packaging with tall vertical interconnects for 5G wireless communication," *IEEE Trans. Antennas Propag.*, vol. 69, no. 10, pp. 6906–6911, Oct. 2021.

[5] S.-S. Hsu, K.-C. Wei, C.-Y. Hsu, and H. Ru-Chuang, "A 60-GHz millimeter-wave CPW-Fed Yagi antenna fabricated by using 0.18-μm CMOS technology," *IEEE Electron Device Lett.*, vol. 29, no. 6, pp. 625–627, Jun. 2008.

[6] S. Zihir, O. D. Gurbuz, A. Kar-Roy, S. Raman, and G. M. Rebeiz, "60-GHz 64- and 256-elements wafer-scale phased-array transmitters using full-reticle and subreticle stitching techniques," *IEEE Trans. Microw. Theory Techn.*, vol. 64, no. 12, pp. 4701–4719, Dec. 2016.

[7] Y. Yu, Z. Akhter, and A. Shamim, "Ultra-thin artificial magnetic conductor for gain-enhancement of antenna-on-chip," *IEEE Trans. Antennas Propag.*, vol. 70, no. 6, pp. 4319–4330, Jun. 2022.

[8] S. Kong, K. M. Shum, C. Yang, L. Gao, and C. H. Chan, "Wide impedance-bandwidth and gain-bandwidth terahertz on-chip antenna with chip-integrated dielectric resonator," *IEEE Trans. Antennas Propag.*, vol. 69, no. 8, pp. 4269–4278, Aug. 2021.

[9] S. Y. Lee, D. Choi, Y. Youn, and W. Hong, "Electrical characterization of highly efficient, optically transparent nanometers-thick unit cells for antenna-on-display applications," in *IEEE MTT-S Int. Microw. Symp. Dig.*, Philadelphia, PA, USA, Jun. 2018, pp. 1043–1045.

[10] J. Park, S. Y. Lee, J. Kim, D. Park, W. Choi, and W. Hong, "An optically invisible antenna-on-display concept for millimeter-wave 5G cellular devices," *IEEE Trans. Antennas Propag.*, vol. 67, no. 5, pp. 2942–2952, May 2019.

[11] W. Hong, J. Choi, D. Park, M. Kim, C. You, D. Jung, and J. Park, "mmWave 5G NR cellular handset prototype featuring optically invisible beamforming antenna-on-display," *IEEE Commun. Mag.*, vol. 58, no. 8, pp. 54–60, Aug. 2020.

[12] *6G the Next Hyper-Connected Experience for All*, Samsung Res., Samsung Electron., Suwon-si, South Korea, 2021.

[13] *Roadmap to 6G*, Next G Alliance, Washington, DC, USA, 2022.

[14] *5G Evolution and 6G*, NTT DoCoMo, Tokyo, Japan, 2020.

[15] *White Paper on 6G Vision and Candidate Technologies*, IMT-2030 (6G) Promotion Group, China, 2021.

[16] *Communications in the 6G Era*, Nokia Bell Labs, Espoo, Finland, 2020.

[17] *White Paper on Broadband Connectivity in 6G*, Univ. Oulu, Oulu, Finland, 2020.

[18] *6G Wireless a New Strategic Vision*, Univ. Surrey, Guildford, U.K., 2020.

[19] *6G Insight: Vision and Technologies*, ETRI, Daejeon, South Korea, 2020.

[20] T. S. Rappaport, "Millimeter wave mobile communications for 5G cellular: It will work!" *IEEE Access*, vol. 1, pp. 335–349, 2013.

[21] X. Tan, Z. Sun, J. M. Jornet, and D. Pados, "Increasing indoor spectrum sharing capacity using smart reflect-array," in *Proc. IEEE Int. Conf. Commun. (ICC)*, Kuala Lumpur, Malaysia, May 2016, pp. 1–6.

[22] J.-B. Gros, V. Popov, M. A. Odit, V. Lenets, and G. Lerosey, "A reconfigurable intelligent surface at mmWave based on a binary phase tunable metasurface," *IEEE Open J. Commun. Soc.*, vol. 2, pp. 1055–1064, 2021.

[23] V. Arun and H. Balakrishnan, "RFocus: Beamforming using thousands of passive antennas," in *Proc. 17th Usenix Conf. Netw. Syst. Des. Implement. (NSDI)*, Santa Clara, CA, USA, Feb. 2020, pp. 1047–1062.

[24] X. Tan, Z. Sun, D. Koutsonikolas, and J. M. Jornet, "Enabling indoor mobile millimeter-wave networks based on smart reflect-arrays," in *Proc. IEEE Conf. Comput. Commun.*, Apr. 2018, pp. 270–278.

[25] M. Dunna, C. Zhang, D. Sievenpiper, and D. Bharadia, "ScatterMIMO: Enabling virtual MIMO with smart surfaces," in *Proc. 26th Annu. Int. Conf. Mobile Comput. Netw. (MobiCom)*, vol. 10, London, U.K., Sep. 2020, pp. 1–14.

[26] X. Pei, "RIS-aided wireless communications: Prototyping, adaptive beamforming, and indoor/outdoor field trials," *IEEE Trans. Commun.*, vol. 69, no. 12, pp. 8627–8640, Dec. 2021.

[27] J. C. Liang, Q. Cheng, Y. Gao, C. Xiao, S. Gao, L. Zhang, S. Jin, and T. J. Cui, "An angle-insensitive 3-bit reconfigurable intelligent surface," *IEEE Trans. Antennas Propag.*, early access, Dec. 1, 2021, doi: 10.1109/TAP.2021.3130108.

[28] X. Meng, M. Nekovee, and D. Wu, "The design and analysis of electronically reconfigurable liquid crystal-based reflectarray metasurface for 6G beamforming, beamsteering, and beamsplitting," *IEEE Access*, vol. 9, pp. 155564–155575, 2021.

[29] E. Baladi, M. Y. Xu, N. Faria, J. Nicholls, and S. V. Hum, "Dual-band circularly polarized fully reconfigurable reflectarray antenna for satellite applications in the Ku-band," *IEEE Trans. Antennas Propag.*, vol. 69, no. 12, pp. 8387–8396, Dec. 2021, doi: 10.1109/TAP.2021.3090577.

[30] E. Carrasco and J. Perruisseau-Carrier, "Reflectarray antenna at terahertz using graphene," *IEEE Antennas Wireless Propag. Lett.*, vol. 12, pp. 253–256, 2013.

[31] R. L. Schmid, D. B. Shrekenhamer, O. F. Somerlock, A. C. Malone, T. A. Sleasman, and R. S. Awadallah, "S-band GaAs FET reconfigurable reflectarray for passive communications," in *Proc. IEEE Radio Wireless Symp. (RWS)*, San Antonio, TX, USA, Jan. 2020, pp. 91–93.

[32] R. Matos and N. Pala, "VO2-based ultra-reconfigurable intelligent reflective surface for 5G applications," *Sci. Rep.*, vol. 12, p. 4497, Mar. 2022.

[33] E. Basar, M. D. Renzo, J. D. Rosny, M. Debbah, M. Alouini, and R. Zhang, "Wireless communications through reconfigurable intelligent surfaces," *IEEE Access*, vol. 7, pp. 116753–116773, 2019.

[34] M. D. Renzo, "Reconfigurable intelligent surfaces vs. relaying: Differences, similarities, and performance comparison," *IEEE Open J. Commun. Soc.*, vol. 1, pp. 798–807, 2020.

[35] Q. Wu and R. Zhang, "Towards smart and reconfigurable environment: Intelligent reflecting surface aided wireless network," *IEEE Commun. Mag.*, vol. 58, no. 1, pp. 106–112, Jan. 2020.

[36] C. Huang, A. Zappone, G. C. Alexandropoulos, M. Debbah, and C. Yuen, "Reconfigurable intelligent surfaces for energy efficiency in wireless communication," *IEEE Trans. Wireless Commun.*, vol. 18, no. 8, pp. 4157–4170, Aug. 2019.

[37] M. A. El Mossallamy, H. Zhang, L. Song, K. G. Seddik, Z. Han, and G. Y. Li, "Reconfigurable intelligent surfaces for wireless communications: Principles, challenges, and opportunities," *IEEE Trans. Cogn. Commun. Netw.*, vol. 6, no. 3, pp. 990–1002, Sep. 2020.

[38] Q. Wu, S. Zhang, B. Zheng, C. You, and R. Zhang, "Intelligent reflecting surface-aided wireless communications: A tutorial," *IEEE Trans. Commun.*, vol. 69, no. 5, pp. 3313–3351, May 2021.

[39] L. Dai, "Reconfigurable intelligent surface-based wireless communications: Antenna design, prototyping, and experimental results," *IEEE Access*, vol. 8, pp. 45913–45923, 2020.

[40] K. Zhi, C. Pan, and K. Wang, "Statistical CSI-based design for reconfigurable intelligent surface-aided massive MIMO systems with direct links," *IEEE Wireless Commun. Lett.*, vol. 10, no. 5, pp. 1128–1132, Feb. 2021.

[41] Q. Zhang, Y. Liang, and H. V. Poor, "Reconfigurable intelligent surfaces assisted MIMO symbiotic radio networks," *IEEE Trans. Wireless Commun.*, vol. 69, no. 7, pp. 4832–4846, Mar. 2021.

[42] A. Papazafeiropoulous, C. Pan, P. Kourtessis, S. Chatzinotas, and J. M. Senior, "Intelligent reflecting surface-assisted MU-MISO systems with imperfect hardware: Channel estimation and beamforming design," *IEEE Trans. Wireless Commun.*, vol. 21, no. 3, pp. 2077–2092, Mar. 2022.

[43] S. Sun and H. Yan, "Channel estimation for reconfigurable intelligent surface-assisted wireless communications considering Doppler effect," *IEEE Wireless Commun. Lett.*, vol. 10, no. 4, pp. 790–794, Jun. 2021.

[44] F. H. Danufane, M. D. Renzo, J. de Rosny, and S. Tretyakov, "On the path-loss of reconfigurable intelligent surfaces: An approach based on green's theorem applied to vector fields," *IEEE Trans. Commun.*, vol. 69, no. 8, pp. 5573–5592, Aug. 2021.

[45] W. Tang, "Wireless communications with reconfigurable intelligent surface: Path loss modeling and experimental measurement," *IEEE Trans. Wireless Commun.*, vol. 20, no. 1, pp. 421–439, Jan. 2021.

[46] G. Gradoni and M. D. Renzo, "End-to-end mutual coupling aware communication model for reconfigurable intelligent surface: An electromagnetic-compliant approach based on mutual impedances," *IEEE Wireless Commun. Lett.*, vol. 10, no. 5, pp. 938–942, Jun. 2021.

[47] M. Najafi, V. Jamali, R. Schober, and H. V. Poor, "Physics-based modeling and scalable optimization of large intelligent reflecting surfaces," *IEEE Trans. Wireless Commun.*, vol. 69, no. 4, pp. 2673–2691, Apr. 2021.

[48] V. Jamali, M. Najafi, R. Schober, and H. V. Poor, "Power efficiency, overhead, and complexity tradeoff of IRS codebook design—Quadratic phase-shift profile," *IEEE Commun. Lett.*, vol. 25, no. 6, pp. 2048–2052, Jun. 2021.

[49] W. L. Stutzman and G. A. Thiele, *Antenna Theory and Design*. New York, NY, USA: Wiley, 2012.

[50] H. Kaouach, L. Dussopt, R. Sauleau, and T. Koleck, "Design and demonstration of 1-bit and 2-bit transmit-arrays at X-band frequencies," in *Proc. Eur. Microw. Conf. (EuMC)*, 2009, pp. 918–921.

[51] J. Budhu and Y. Rahmat-Samii, "Understanding the appearance of specular reflection in offset fed reflectarray antennas," in *Proc. IEEE Int. Symp. Antennas Propag. (APSURSI)*, Jul. 2011, pp. 97–100.

[52] J. G. Jeong, N. J. Park, and Y. J. Yoon, "Aperture efficiency improvement of folded reflectarray using rectangle and split-ting combined element," *Electron. Lett.*, vol. 53, no. 13, pp. 797–798, 2018.

[53] F. Venneri, S. Costanzo, and G. Di Massa, "Design and validation of a reconfigurable single varactor-tuned reflectarray," *IEEE Trans. Antennas Propag.*, vol. 61, no. 2, pp. 635–645, Feb. 2013.

[54] S. V. Hum, M. Okoniewski, and R. J. Davies, "Modeling and design of electronically tunable reflectarrays," *IEEE Trans. Antennas Propag.*, vol. 55, no. 8, pp. 2200–2210, Aug. 2007.

[55] G. Perez-Palomino, P. Baine, R. Dickie, M. Bain, J. A. Encinar, R. Cahill, M. Barba, and G. Toso, "Design and experimental valication of liquid crystal-based reconfigurable reflectarray element with improved bandwidth in F-band," *IEEE Trans. Antennas Propag.*, vol. 61, no. 4, pp. 1704–1713, Apr. 2013.

[56] H. Kim, J. Kim, and J. Oh, "Liquid-crystal-based X-band reactively loaded reflectarray unit cell to reduce reflection loss," *IEEE Antennas Wireless Propag. Lett.*, vol. 20, no. 10, pp. 1898–1902, May 2021.

[57] H. Kamoda, T. Iwasaki, J. Tsumochi, T. Kuki, and O. Hashimoto, "60-GHz electronically reconfigurable large reflectarray using single-bit phase shifters," *IEEE Trans. Antennas Propag.*, vol. 59, no. 7, pp. 2524–2531, Jul. 2011.

[58] J. Han, L. Li, G. Liu, Z. Wu, and Y. Shi, "A wideband 1 bit 12×12 reconfigurable beam-scanning reflectarray: Design, fabrication and measurement," *IEEE Antennas Wireless Propag. Lett.*, vol. 18, no. 6, pp. 1268–1272, Mar. 2019.

JUNGI JEONG received the B.S. degree in electronic engineering from Kwangwoon University, Seoul, South Korea, in 2013, and the Ph.D. degree in electrical and electronic engineering from Yonsei University, Seoul, in 2019.

From September 2019 to July 2020, he worked at the Network Division of Samsung Electronics, and developed antennas for 5G base stations. He is currently working with the 6G Research Team, Samsung Research, Seoul, and serves as an RF/Antenna Engineer investigating B5G/6G communications, sub-THz antenna-in-package (AiP) technology, and reconfigurable intelligent surfaces (RISs). His research interests include millimeter/THz wave antennas, metamaterials, metasurfaces, lenses, reflectarrays, wave propagation, and antenna measurement.

Dr. Jeong received the Minister Prize from the Ministry of Science and ICT, South Korea, in 2018; the Outstanding Student Fellow from Yonsei University, in 2017; the Outstanding Research Award from the Asian Workshop on Antennas, in 2016; and the Student Presentation Award from the IEEE International Workshop on Electromagnetics, in 2018.

JUN HWA OH received the B.S. and M.S. degrees in electric and electronic engineering from Yonsei University, Seoul, South Korea, in 2007 and 2009, respectively.

In 2009, he joined Samsung Electronics as an Antenna Engineer. He worked in the Mobile-eXperience (MX) division for ten years and developed mobile phone antennas for 2G/3G/4G/5G communications and WiFi, Bluetooth, and GPS connectivity. Since 2019, he has been working as a Principal Engineer with the 6G Research Team, Samsung Research, Seoul. He is currently developing advanced antenna and metamaterial technologies for B5G/6G communication systems, including sub-terahertz antenna-in-package (AiP) technology and reconfigurable intelligent surfaces (RISs). His research interests include electromagnetic wave propagation, antenna design and measurement, reconfigurable antennas, microwave/RF circuits, and computational electromagnetics.

YUNTAE PARK received the B.S. degree in electronics system engineering from Hanyang University, Ansan, South Korea, in 2018, and the M.S. degree in electronics and computer engineering from Hanyang University, Seoul, South Korea, in 2020.

Since 2020, he has been working with Samsung Research, Seoul, where he serves as an RF/Antenna Engineer researching sub-THz antenna design and mmWave reconfigurable intelligent surfaces (RISs). His research interests include the electromagnetic analysis of antennas and metamaterials for B5G/6G communications, including sub-THz antenna-in-package (AiP) technology, reconfigurable intelligent surfaces (RISs), metasurfaces, lenses, and antenna measurements.

SEUNG YOON LEE received the B.S. degree in computer and communication engineering from Korea University, Seoul, South Korea, in 2016, and the M.S. degree in electrical engineering from the Pohang University of Science and Technology (POSTECH), Pohang, South Korea, in 2018. He is currently pursuing the Ph.D. degree in electrical engineering with the Georgia Institute of Technology, Atlanta, GA, USA.

From July 2018 to October 2020, he was employed as a Semiconductor/RF Engineer at SK Hynix, Icheon, South Korea, working as a Device Modeling Engineer, participating in numerous cutting-edge SPICE memory model extractions, and designing on-chip inductors for high-speed memory products. Since September 2020, he has been working with Samsung Research, Seoul, where he serves as an RF/Antenna Engineer researching sub-THz antenna designs, mmWave reconfigurable intelligent surfaces (RISs), and antenna probe station equipment. He has published two international journal papers, one domestic journal paper, and five international conference papers. His current research interests include the technical analysis of antennas and metamaterials for B5G/6G communications (e.g., sub-THz antenna-in-package technology) and designing a mmWave RIS for upcoming next-generation communication technologies. He is recognized as the Inventor of 20 patents pertaining to his research topics.

Mr. Lee was a Recipient of several awards and honors, including the Class of 2018 Outstanding Master's Thesis Award from POSTECH, and the 1st Prize Best Paper Student Award from the IEEE International Symposium on Antennas and Propagation, 2018.

SANG-HYUK WI received the M.S. and Ph.D. degrees in electrical and electronic engineering from Yonsei University, Seoul, South Korea, in 2003 and 2008, respectively.

In 2009, he joined Samsung Electronics and worked on antenna development for 4G LTE mobile devices. In 2011, he joined the 802.11 a/b/g/n Chipset Development Project as a Chipset Evaluation and a Wireless Connectivity System Design Engineer. From 2013 to 2017, he was employed in the Visual Display division, working on the development of wireless connectivity modules such as Wi-Fi, Bluetooth, and Wi-Fi/Bluetooth combos for smart TVs. In July 2017, he joined Samsung Research and worked on the wireless power transfer system design. Since 2020, he has been with the 6G Research Team, working in a 5G and 6G antenna development. His research interests include phased-array antennas, miniaturized antennas, antenna-in-package (AiP) technology, reconfigurable intelligent surfaces (RISs), and RF systems.

• • •